

Understanding the Roles of Tris(trimethylsilyl) Phosphite (TMSPi) in LiNi_{0.8}Mn_{0.1}Co_{0.1}O₂ (NMC811)/Silicon–Graphite (Si–Gr) Lithium-Ion Batteries

Haidong Liu, Andrew J. Naylor, Ashok Sreekumar Menon, William R. Brant, Kristina Edström, and Reza Younesi*

The coupling of nickel-rich LiNi_{0.8}Mn_{0.1}Co_{0.1}O₂ (NMC811) cathodes with high-capacity silicon–graphite (Si–Gr) anodes is one promising route to further increase the energy density of lithium-ion batteries. Practically, however, the cycle life of such cells is seriously hindered due to continuous electrolyte degradation on the surfaces of both electrodes. In this study, tris(trimethylsilyl) phosphite (TMSPi) is introduced as an electrolyte additive to improve the electrochemical performance of the NMC811/Si–Gr full cells through formation of protective surface layers at the electrode/electrolyte interfaces. This is thought to prevent the surface fluorination of the active materials and enhance interfacial stability. Notably, TMSPi is shown to significantly reduce the overpotential and operando X-ray diffraction (XRD) confirms that an irreversible “two-phase” transition reaction caused by the formed adventitious Li₂CO₃ layer on the surface of NMC811 can transfer to a solid-solution reaction mechanism with TMSPi-added electrolyte. Moreover, influences of TMSPi on the cathode electrolyte interphase (CEI) on the NMC811 and solid electrolyte interphase (SEI) on the Si–Gr are systematically investigated by electron microscopy and synchrotron-based X-ray photoelectron spectroscopy which allows for the nondestructive depth-profiling analysis of chemical compositions and oxidation states close to the electrode surfaces.

For the next-generation LIBs, development of the novel cathode materials with increased reversible capacity and/or high operating voltage is pursued. Nickel-rich layered LiNi_xMn_yCo_{1-x-y}O₂ (NMC, $x \geq 0.5$) cathode materials have gained significant attention, owing to their higher reversible capacity with the increase of Ni content at the same cut-off voltage.^[2,3] It is believed that the structural stability of various NMC materials is highly dependent on the Li⁺ extraction ratio, which can be controlled by the specific charge capacity and/or the upper cut-off voltage. Nickel-rich materials have become the state-of-the-art cathode materials in commercial LIBs for automotive applications, demonstrating substantially improved energy density.^[4,5] In particular, LiNi_{0.8}Mn_{0.1}Co_{0.1}O₂ (NMC811), with a high capacity of ≈ 200 mAh g⁻¹ and reduced amount of cobalt, is one of the most promising candidates to achieve higher energy density LIBs.^[6] Despite this, NMC811 experiences a limited cycle

1. Introduction

Advanced lithium-ion batteries (LIBs) have expanded their large-scale application from portable electronic devices toward the electric vehicles market in recent years.^[1] The ever-growing demand of gravimetrically and volumetrically energy densities of LIBs has accelerated the development of high-capacity cathode and anode active materials.

life in practical applications due to a number of influencing factors. These include a high sensitivity toward moisture/air, gas evolution, crack generation, and surface instability caused by the presence of highly oxidizing Ni⁴⁺ at the delithiated state, resulting in electrolyte oxidation/decomposition.^[7,8] These issues are often triggered at the particle surfaces or at the cathode-electrolyte interface, and then result in further deterioration of the overall performance. Hence, it is crucial to stabilize the cathode-electrolyte interface to achieve enhanced electrochemical performance when employing NMC811.

The desire to increase the energy density of LIBs also drives the development of high-capacity anode materials, such as silicon and silicon-based materials (3579 mAh g⁻¹ for Li₁₅Si₄), to replace the conventional graphite (372 mAh g⁻¹ for LiC₆).^[9–11] The practical application of pure Si as an anode material is hampered by rapid capacity fading, resulting from its large volume change (up to $\approx 300\%$) and consequential continuous electrolyte decomposition onto freshly exposed Si surfaces during the repeated lithiation/delithiation processes.^[11–14] Recently, silicon–graphite (Si–Gr) composites have been utilized as a trade-off to balance the advantages of the increased capacity of Si and the high stability of graphite electrode to limit the undesired volume change during cycling.^[15–21] Although sacrificing

Dr. H. Liu, Dr. A. J. Naylor, A. S. Menon, Dr. W. R. Brant, Prof. K. Edström, Dr. R. Younesi
 Department of Chemistry – Ångström Laboratory
 Uppsala University
 Box 538, Uppsala 75121, Sweden
 E-mail: reza.younesi@kemi.uu.se

 The ORCID identification number(s) for the author(s) of this article can be found under <https://doi.org/10.1002/admi.202000277>.

© 2020 The Authors. Published by WILEY-VCH Verlag GmbH & Co. KGaA, Weinheim. This is an open access article under the terms of the Creative Commons Attribution License, which permits use, distribution and reproduction in any medium, provided the original work is properly cited.

DOI: 10.1002/admi.202000277

capacity, the inclusion of graphite can furthermore serve as a conductive framework to provide electronic conductivity to the Si particles, thereby enhancing the overall electrochemical performance at a low cost. Nevertheless, the severe volume change of Si can give rise to an unstable anode-electrolyte interface between the Si-Gr anode and electrolyte during cycling, leading to the continuous consumption of Li^+ , side reactions, and durability problems.^[22] So, it is also a determining factor to create a stable and robust anode-electrolyte interface to improve cycling stability of the Si-Gr anode.

The instability of electrode-electrolyte interfaces for both NMC811 cathode and Si-Gr anode is one of the most serious issues to address for their further implementation in high energy-density LIBs. Extensive efforts have been made to search for efficient electrolyte additives or develop new electrolyte systems to enhance the interfacial stability between the electrode and electrolyte. The incorporation of small amounts of additives in the electrolyte has been considered as one of the most effective ways to form a stable cathode-electrolyte interphase (CEI) at the cathode-electrolyte interface and the solid-electrolyte interphase (SEI) at the anode-electrolyte interface.

For NMC811 cathode, especially when operated at high upper cut-off voltages (i.e., ≥ 4.5 V vs Li/Li^+), a stable CEI for preventing excessive electrolyte oxidization, transition metal dissolution, and interfacial impedance rise is critical. The CEI can greatly affect overall cell operation and efficiency. Various electrolyte additives have been employed to tune the composition and structure of the CEI to obtain a stable and robust interphase.^[23–26] For example, Li et al. tailored a boron-oxygen-rich CEI on a Ni-rich cathode by adding 1.5% lithium bis(oxalate) borate (LiBOB) to the electrolyte, which significantly suppressed side reactions at the Ni-rich surface and increased Li^+ ion diffusivity.^[26] Indeed, a small amount of electrolyte additive can effectively promote the cycling stability of Ni-rich cathode materials.

For the Si-based anode, the severe volume change prevents the formation of a stable SEI. Likewise, electrolyte additives can greatly influence both the morphology and composition of the SEI on Si-based anodes.^[27,28] Vinylene carbonate, fluoroethylene carbonate (FEC), tris(pentafluorophenyl)borane undergo reductive decomposition at the surface of Si-Gr anodes at higher potential than the commonly used ethylene carbonate (EC). They have been used in various quantities as electrolyte additives to improve cycling performance by tuning the growth and composition of SEI.^[29–31] For example, FEC can improve the Coulombic efficiency and capacity retention of Si-based anodes, since it induces the formation of a conformal SEI to effectively limit the generation of large cracks and preserve the original surface morphology.^[30] Therefore, it is an efficient approach to improve the stability of the CEI/SEI and other properties of the cells through employing functional additives without altering too much physical properties of the electrolyte.^[8,32]

The development of an appropriate additive, which is compatible with both NMC811 cathode and Si-Gr anode, proves to be a considerable challenge. Recently, phosphites ($\text{P}(\text{OR})_3$), phosphates ($\text{OP}(\text{OR})_3$) derivatives, such as tris(trimethylsilyl) phosphite (TMSPi) and tris(trimethylsilyl) phosphate (TTSP), have been developed as film-forming protective agents for application with different Ni-rich materials.^[33–35] For example, previous reports showed that TMSPi, which was able to

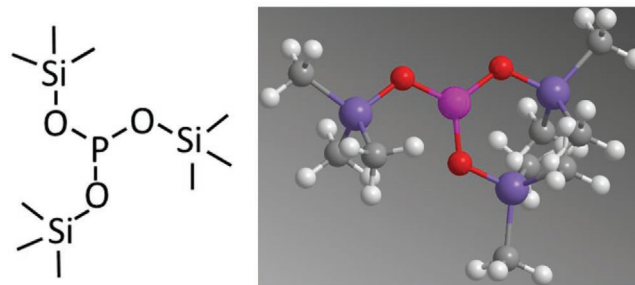


Figure 1. 2D and 3D structures of tris(trimethylsilyl) phosphite (TMSPi).

substantially improve stability of NMC111/graphite, NMC/442/graphite, or NMC532/graphite cells, failed to adequately enhance the NMC811/graphite cell performance.^[8,36] Combination of TMSPi with other additives was more effective than using a single additive by providing multiple functions at the Ni-rich cathodes, but a clear understanding of the mechanisms for such improvements was not demonstrated.^[36] It was also shown that the use of TMSPi effectively alleviated the hydrolysis of LiPF_6 and acted as a hydrogen fluoride (HF) scavenger through breaking of O–Si bonds, slowing the impedance increase.^[37–39] Furthermore, TMSPi has been used as an efficient additive to improve the surface stability of the graphite anode. However, the studies on the effects of TMSPi in combination with Si-based anode materials are lacking.

In this contribution, TMSPi as an electrolyte additive is firstly introduced and investigated for the application in the NMC811/Si-Gr full cells between 2.7 and 4.4 V at room temperature (RT). The 2D and 3D chemical structure of TMSPi is illustrated in **Figure 1**. The roles of 2 wt% of TMSPi was investigated by correlating the electrochemical behaviors of the NMC811/Li half and NMC811/Si-Gr full cells with structural evolution of NMC811 examined by operando X-ray diffraction (XRD), surface morphology observed by scanning electron microscopy (SEM), and surface chemistry determined by synchrotron-based X-ray photoelectron spectroscopy (XPS) depth profiling analysis. Galvanostatic cycling measurements and electrochemical impedance spectroscopy (EIS) as well as storage experiments were used to emphasize the improvement on electrochemical performance resulting from the use of TMSPi. The electrode morphology as well as the chemical composition and thickness of the CEI and SEI formed at the surfaces of both NMC811 cathodes and Si-Gr anodes after formation cycles and long cycling were determined to understand the role of TMSPi on the electrochemical performance of NMC811/Gr full cells.

2. Result and Discussion

2.1. Electrochemical Behaviors

2.1.1. Influence of TMSPi Additive on the Electrolyte Stability

As reported, TMSPi has a lower oxidation stability than the solvent ethylene carbonate (EC) in the electrolyte, meaning it will be oxidized before EC and contribute to the passivating CEI formed at the cathode surface.^[37,40,41] To confirm this, linear sweep voltammetry (LSV) was performed with the baseline

electrolyte and 2 wt% TMSPi, respectively, as displayed in Figure S1 (Supporting Information). The addition of TMSPi decreases the oxidation stability of the new electrolyte system with a strong anodic current appearing at ≈ 4.2 V (vs Li/Li⁺). The observed current is most likely caused by the electrochemical oxidation of the TMSPi, which confirms that TMSPi oxidizes preferentially to EC and DEC in the electrolyte. Importantly, the further oxidation potential of the electrolyte postpones from ≈ 4.7 to 5.0 V, indicating that the preferential oxidation of TMSPi results in the suppression of the baseline electrolyte at high potential (>4.7 V), which is necessary for the practical application of the most cathode under high voltage.

Cyclic voltammetry (CV) for Si–Gr anodes in the two electrolytes with and without TMSPi was performed as shown in Figure S2 (Supporting Information). From the measurements, the onset potential for electrolyte reduction was arbitrarily defined as the potential at which the specific current reached 0.003 mA mg⁻¹. The addition of TMSPi to the baseline electrolyte results in a shift of the onset potential for electrolyte reduction to a higher value from 0.94 to 0.99 V in the first cycle, suggesting the reductive decomposition of TMSPi prior to the electrolyte solvent molecules, effectively reducing the electrolyte decomposition in the ongoing scan. As denoted by the reduction/oxidation current curves, the sharp increase of current density during lithiation in the first reductive scan in the 2 wt% TMSPi electrolyte starts at ≈ 0.2 V versus Li/Li⁺ compared with ≈ 0.15 V versus Li/Li⁺ in the baseline electrolyte. It also reveals that the lithiation feature of Si and Gr in the first cycle were largely superimposed during the reductive scan at potential below 0.15 V for the baseline electrolyte, while an evident reduction peak at ≈ 0.17 V can still be observed for the TMSPi electrolyte. Therefore, the addition of TMSPi has a strong impact on the lithiation/delithiation behavior of Si–Gr anodes. We note that there is a controversy over the reduction stability of the TMSPi additive from the previous reports. The theoretical calculations of redox potentials conducted by Han et al. suggested that TMSPi has a considerably lower reduction potential than that of EC, and would not even be reduced at the anode.^[37] However, Tornheim et al. show that a reduction peak appeared at higher value than that of EC, which indicates that TMSPi is reduced earlier than EC while TMSPi and/or its decomposition products can contribute to the SEI formation.^[35] It is also revealed by Qi et al. that the position (or absence) of such a reduction peak depends on the storage time of the electrolyte, where the reduction is only observed for the fresh electrolyte since TMSPi has a limited lifetime.^[33] Furthermore, chemical and electrochemical crosstalk is possible between the cathode and anode.^[42,43] The electrochemical oxidation products of TMSPi at the cathode can migrate and induce subsequent reactions at the anode. Therefore, the validity of the redox stability data of electrolytes can be considered as questionable, since it is uncertain whether the obtained results can be transferred from the LSV/CV measurement setups to a practical setup of full cells, as discussed in a previous report.^[44]

2.1.2. NMC811–Li and Si–Gr/Li Half Cells

Figure 2a depicts the first charge/discharge curves of NMC811/Li cells with the baseline and 2 wt% TMSPi electrolytes at 0.1 C

between 3 and 4.5 V. The cycling performance of NMC/Li half cells with two electrolytes is shown in Figure S3a (Supporting Information). The first charge and discharge capacities of the cell with the baseline electrolyte are 239 and 210 mAh g⁻¹, respectively, corresponding to a Coulombic efficiency of 87.9%. As for the cell with 2 wt% TMSPi electrolyte, the charge and discharge capacities are increased slightly to 243 and 214 mAh g⁻¹, respectively, with a CE of 88.1%. While Coulombic efficiency is nearly identical and the charge/discharge capacities are only slightly increased, the cell polarization with the TMSPi electrolyte is significantly reduced. For the NMC811 in the baseline electrolyte, there is a steep increase of the voltage up to 3.85 V in the early stage of the charge (see inset in Figure 2a). The voltage then subsequently decreased to a plateau at 3.78 V after the capacity reached ≈ 20 mAh g⁻¹. This overpotential in the first charge is mainly caused by the adventitious Li₂CO₃ layer formed at the cathode particle surface during material storage and/or electrode handling due to the moisture/air sensitivity, which has been proved in the previous report.^[45] This adventitious Li₂CO₃ layer impedes ionic and electronic transportation. Remarkably, it seems that the TMSPi additive could remove the adventitious Li₂CO₃ layer on the electrode particle surface, leading to significantly reduced polarization and increased the reversible capacity during the initial cycle. The induced effect on the electrochemical kinetics by TMSPi influences the nature of the observed phase transition in NMC811, which is investigated in this work by operando XRD and will be discussed in the next section. The reduced overpotential is highly meaningful for practical applications because the energy efficiency of the cell with the TMSPi electrolyte is significantly improved due to the increased discharge voltage.^[46] From the second cycle as shown in Figure 2b, the severe overpotential during the charge process of the cell with the baseline electrolyte is greatly reduced and the charge/discharge curves are almost identical, although with slightly lower capacity than for the cell with the TMSPi electrolyte.

The cycling performance of Si–Gr/Li half cells with two electrolytes is exhibited in Figure S3b (Supporting information). Figure 2c shows that the initial lithiation/delithiation profiles of the Si–Gr/Li half cells with the baseline and 2 wt% TMSPi electrolytes. The cell with TMSPi additive has larger initial lithiation/delithiation capacities of 756/677 mAh g⁻¹, compared with 736/659 mAh g⁻¹ for the cell with the baseline electrolyte. The increased capacity is mainly attributed to the decreased overpotential with the TMSPi electrolyte. It can be inferred that TMSPi and/or its decomposition products facilitate the Li⁺ transport through the Si–Gr surface during the lithiation/delithiation processes. Note that the Si–Gr lithiation profiles with the TMSPi electrolyte are distinctly different for the first and second cycles. The first lithiation curves present the major difference because TMSPi is involved when the other solvents (EC/DEC) are reduced to form SEI layer, indicating that the formed SEI contains the TMSPi and/or its reduction products.

2.1.3. NMC811/Si–Gr Full Cells

Galvanostatic cycling of NMC811/Si–Gr full cells with the two electrolytes has been performed, and the results are presented

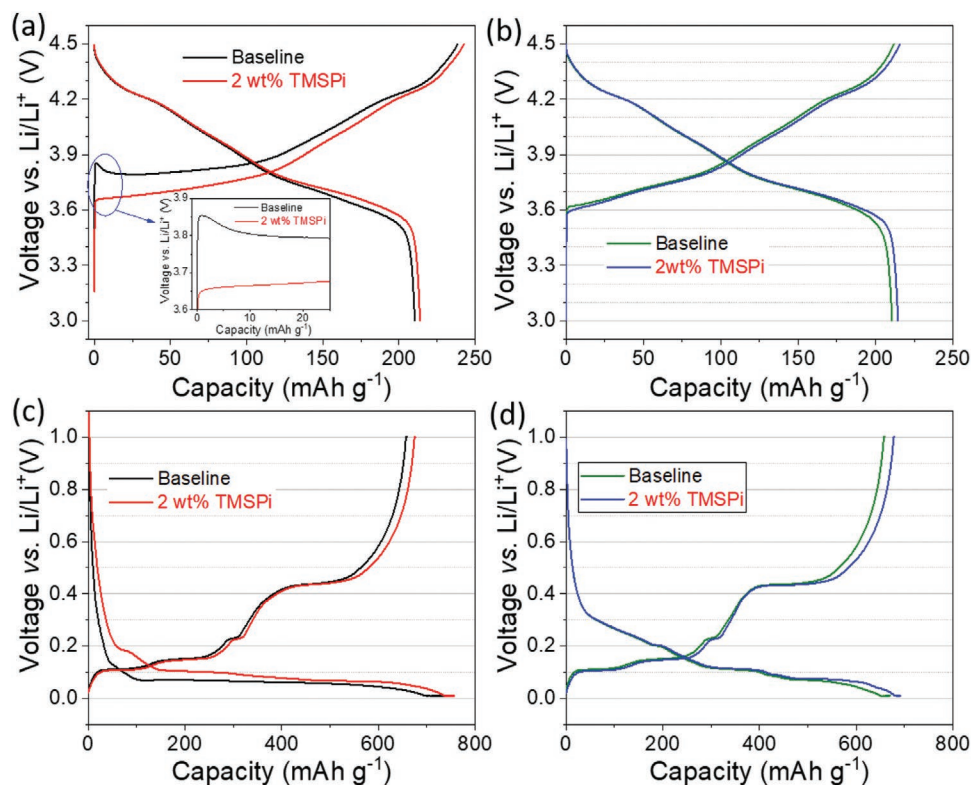


Figure 2. a) The first and b) second charge/discharge curves of NMC811/Li cells at 0.1 C between 3 and 4.5 V and c) the first and d) second lithiation/delithiation curves of Si-Gr/Li cells at 0.1 C between 0.01 and 1 V in the baseline electrolyte and 2 wt% TMSPi electrolytes, respectively. Inset in (a) shows the enlarged part of early stage of the charge.

in **Figure 3**. At the beginning, considering the possible influence of TMSPi content in the electrolyte on the full cells, the suitable amount of TMSPi were optimized by studying the cycling stability of and 2 wt% TMSPi was selected, see Figure S4 (Supporting Information). Thus, the following discussion focuses only on the influence of 2 wt% TMSPi electrolyte. In terms of long cycling, 2 wt% TMSPi substantially improved the capacity retention and Coulombic efficiency as shown in Figure 3a,b. 80% of capacity (referring to 150 mAh g⁻¹) is retained after 50 cycles at 0.5 C with the TMSPi electrolyte, whereas the cell with the baseline electrolyte has a capacity retention of 55% (108 mAh g⁻¹). Meanwhile, a slightly increased first-cycle Coulombic efficiency of ≈87% is obtained, and relatively higher Coulombic efficiency is retained in following cycles with the TMSPi electrolyte. It indicates that the decomposition of TMSPi on the NMC811 cathode and the Si-Gr anode during the first cycles promotes the formation of stable CEI and SEI, reducing the cell polarization and improving Coulombic efficiency. The corresponding charge/discharge curves for the selected cycles are exhibited in Figure 3d,e, which also demonstrates the stabilization of charge/discharge capacities with the addition of TMSPi. Figure 3c shows the average ΔV for the NMC811/Si-Gr full cells without/with TMSPi during the charge/discharge measurements. Differences in ΔV are caused by differences in cell polarization during cycling and smaller values of ΔV generally suggest lower interfacial impedance. It shows that cells containing the TMSPi electrolyte have much lower ΔV and

thus lower interfacial impedance upon cycling than the cells with the baseline electrolyte. The rate capabilities of NMC811/Si-Gr full cells with/without TMSPi are also demonstrated in Figure 3f. Upon increasing the discharge C-rates from 0.2 to 5 C with a constant charge at 0.2 C after cycling at 0.1 C, the specific capacity retention. The reversible capacity fade behavior at high C-rate discharge depended strongly on the electrolyte. The cell containing TMSPi electrolyte with better rate capability suggests relatively fast Li⁺ transport, which is related with the decreased surface impedance from both cathode and anode. However, limited capacity delivery is presented at sufficiently high C-rate (5 C) of discharge even though the cell impedance was decreased by using TMSPi, which may be caused by the inevitable lithium plating.^[47]

Nyquist plots of the NMC811/Si-Gr full cells with two electrolytes before and after cycling are presented in Figure 3g–i, respectively. The two fresh cells with the baseline and TMSPi electrolyte, respectively, before cycling show one semicircle and a sloped line in Figure 3g. While an additional semicircle appears in the high-frequency region after cycling, which can be ascribed to interfacial impedance. This reveals that electrode/electrolyte interphases are established with both baseline and TMSPi electrolytes. The interfacial impedance with the TMSPi electrolyte is lower than that with the baseline electrolyte after the formation cycles at 0.1 C. As cycling progresses, the interfacial impedance of the two cells both increased, but the cell with TMSPi electrolyte remains lower value. Importantly,

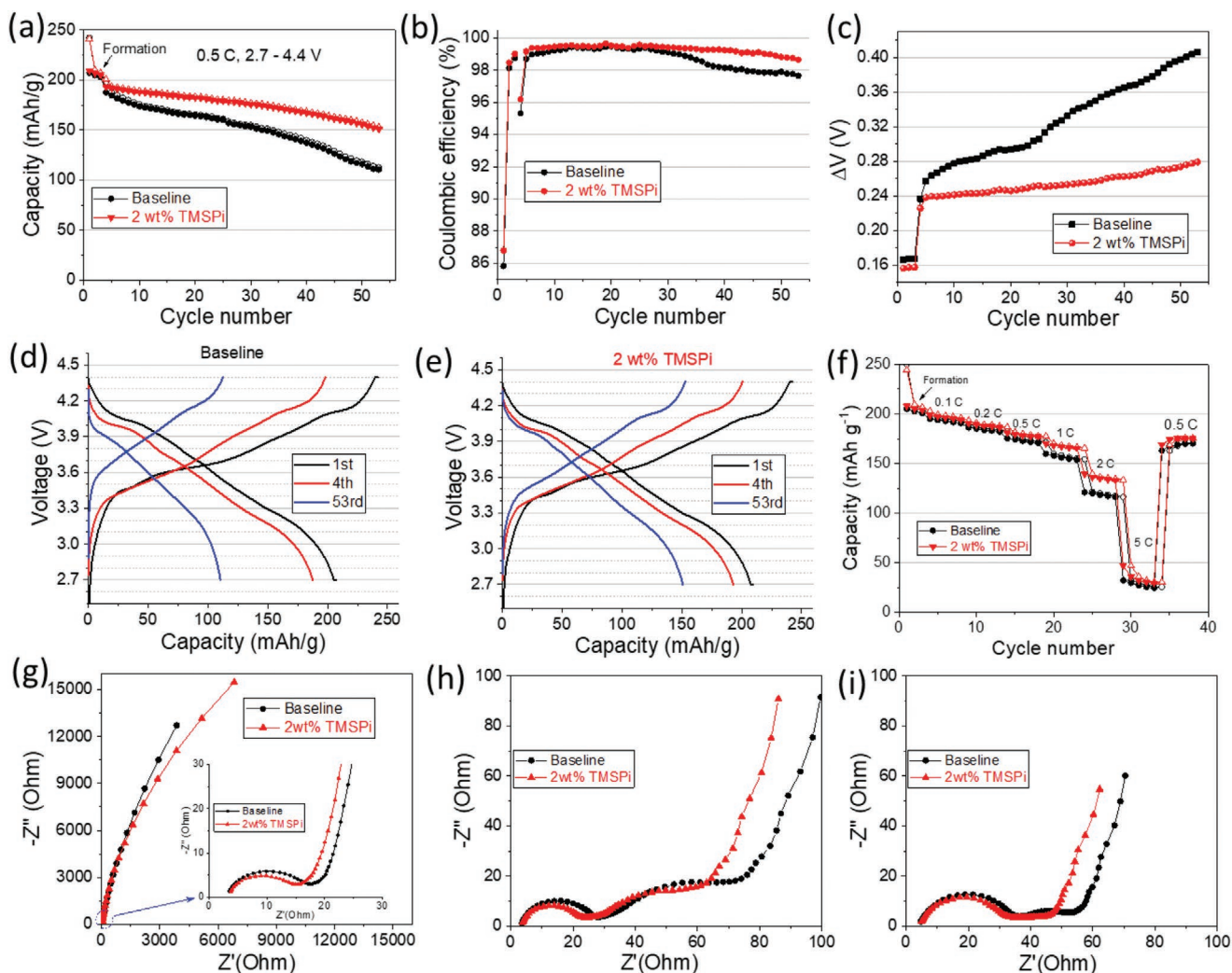


Figure 3. Comparison of the influence of the addition of 2 wt% TMSPi into the baseline electrolyte on the electrochemical behaviors of the NMC811/Si-Gr full cells. Depicted are a) cycling stability and b) the Coulombic efficiencies at 0.5 C in the cut-off voltage of 2.7–4.4 V. c) ΔV (differences between average charge and average discharge voltages) as a function of cycle number. The corresponding charge/discharge curves cycled in the d) baseline electrolyte and e) 2 wt% TMSPi electrolyte. f) Rate capability varied from 0.1 to 5 C with a constant charging rate at 0.2 C after cycling at 0.1 C between 2.7 and 4.4 V. Nyquist plots of the full cells g) before and after h) 3 formation cycles at 0.1 C and i) 50 cycles at 0.5 C, all the cells were measured at discharged state. 1 C = 200 mA g⁻¹.

the charge-transfer resistance after 53 cycles decreases more sharply for the cells with TMSPi. This result implies that the use of TMSPi in the electrolyte contributes to lower full cell resistance that might be related to the stable electrode/electrolyte interphases formed on both cathode and anode throughout cycling. We can see that these impedance results also agree well with the above rate capability.

The lower cell resistance of NMC811/Si-Gr with 2 wt% TMSPi electrolyte suggests that the addition of TMSPi has the capability to enable excellent reversibility of both NMC811 and Si-Gr by forming highly Li⁺ conductive CEI and SEI. The rapid capacity fading and decreased Coulombic efficiency of the full cells with the baseline electrolyte are mainly due to the largely increased cell impedance, which is caused by the formation of unstable and lowly conducting CEI and SEI, inducing continuous consumption of electrolyte on both cathode and anode

sides. More details about the differences in surface chemistry on NMC811 and Si-Gr electrodes cycled with the two electrolytes will be discussed later.

As is well known, parasitic reactions occurring at the electrode/electrolyte interface during storage is a main influencing factor for cell performance degradation. Figure S5 (Supporting Information) shows the storage behavior of the fully charged cell starting at 4.4 V after 500 h, for the baseline and TMSPi electrolyte at room temperature. The two cells display a similar trend, but the cell with TMSPi has smaller voltage drop and retains a higher capacity. The voltage of the cell with TMSPi dropped to 4.08 V, which is better than that of the baseline with 4.04 V, revealing that the storage performance of the full cells can be effectively enhanced by adding TMSPi. This also suggests that TMSPi can improve the interfacial stability of the electrodes in full cells.

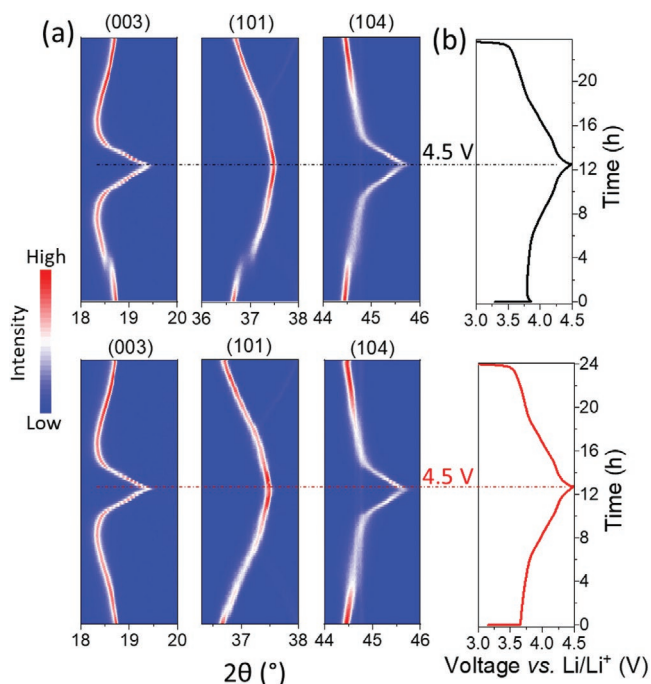


Figure 4. Operando XRD data recorded during the first charge/discharge processes of NMC811/Li cells at C/10 between 3 and 4.5 V with the baseline electrolyte (up) and TMSPi electrolyte (bottom), respectively. a) Contour plots of the selected (003), (101), and (104) diffraction reflections and b) the corresponding charge/discharge profiles. The intensity chart is given at the very left side. 1 C = 200 mA g⁻¹.

2.2. Structural Analysis from Operando XRD

Firstly, the powder XRD and Rietveld refinement (Figure S6, Supporting Information) of the pristine NMC811 material were carefully undertaken to identify the sample structure. The reflections are consistent with the *R-3m* NMC phase, and the structural parameters of the NMC811 obtained from Rietveld refinement are shown in Table S2 (Supporting Information).

Operando XRD data recorded during the first cycle of the NMC811/Li cells with the baseline and 2 wt% TMSPi electrolytes in Figure 4 show striking differences in the structural evolution and electrochemical profiles for identically prepared and cycled NMC811 electrodes, which were handled under the same processing conditions.

The NMC811 electrode cycled with the baseline electrolyte (Figure 4a, top) shows a typical structural evolution, where additional reflections at the early stage of charge, corresponding to the steep increase of the voltage up to 3.85 V as presented in Figure 4b (top, the same curve in Figure 2a). This suggests the formation of an additional rhombohedral phase with similar crystallographic structure as the original NMC811 phase, as reported in the literature.^[45,48] As discussed above, this additional phase forms at the early stage of charge caused by the adventitious Li₂CO₃ layer formed on the NMC811 surface. In contrast, the NMC811 electrode cycled with the TMSPi electrolyte (Figure 4, bottom) behaves as a single-phase solid solution through the entire charge process, rather than a “two-phase” evolution. The different reaction mechanisms can be interpreted by the reaction heterogeneity induced by the formed

adventitious Li₂CO₃ surface layer that hinders the Li⁺ and electron transport for NMC811.^[45] This reveals that this adventitious Li₂CO₃ layer on NMC811 can be broken down in the TMSPi electrolyte, perhaps TMSPi is likely to form an association with the adventitious Li₂CO₃ formed on the cathode particle surface because of coordination effect of TMSPi.^[34,37] This new discovery suggests that TMSPi could serve as a potential Li-residue scavenger. As a result, the impedance and kinetic barriers for Li⁺ transfer during the initial cycle can be largely reduced by using TMSPi electrolyte.

Furthermore, as depicted in Figure S7 (Supporting Information), the continuous decrease of the lattice parameter *a* and concomitant increase of the lattice parameter *c* up to ≈4.1 V is due to electrostatic repulsion of MO₂ layers.^[49] At ≈4.1 V, the decrease of the lattice parameter *c* is caused by the attractive van der Waals interactions.^[50] In general, similar trend for the lattice parameters are observed for NMC811 electrodes cycled in both electrolytes. Herein, the operando XRD study also suggests that the intrinsic phase transition mechanism of NMC811 in a cell could be influenced by the electrode/electrolyte interactions induced by electrolyte additive.

2.3. Analysis of the Interfacial Stability

The chemical and electrochemical decomposition of the electrolyte components on the specific cathode and anode surfaces results in the formation of unique interphases at electrode/electrolyte interfaces, greatly influencing the overall cell performance.^[27,32] Considering this, the evaluation of TMSPi participation in the formation of CEI and SEI on the electrodes is of keen interest. Consequently, SEM was conducted to observe surface morphology changes of the electrodes. Energy-tuned XPS depth profiling analysis is carried out to ascertain the compositions and verify the influences of TMSPi on the performance of NMC811 cathode and Si-Gr anode.

A nondestructive depth profile was obtained by employing synchrotron-based energy-tuned X-ray photoelectron spectroscopy with all electrodes measured using three different energies as described in Table S1 (Supporting Information). Different photon energies were chosen for each core level when performing soft XPS in order to obtain the same kinetic energy of photoelectrons for probing the same depth. The electron inelastic mean free path (IMFP) is extremely sensitive to the kinetic energy of photoelectrons for soft XPS, and different core levels can be probed at the same depth using the same kinetic energy.^[27,51] The kinetic energy selected here is 200 eV, which gives a probing depth of ≈3 nm. For the hard XPS measurements, two photon energies, 2350 and 7050 eV, were adopted, which correspond to probing depths of ≈17 and ≈47 nm, respectively.

2.3.1. Surface Chemistry on the NMC811 Cathode

The morphology of the NMC811 electrode surface with two different electrolytes before and after cycling was visualized by SEM. SEM images of a typical pristine NMC811 electrode and the cycled electrodes with the baseline and TMSPi electrolyte

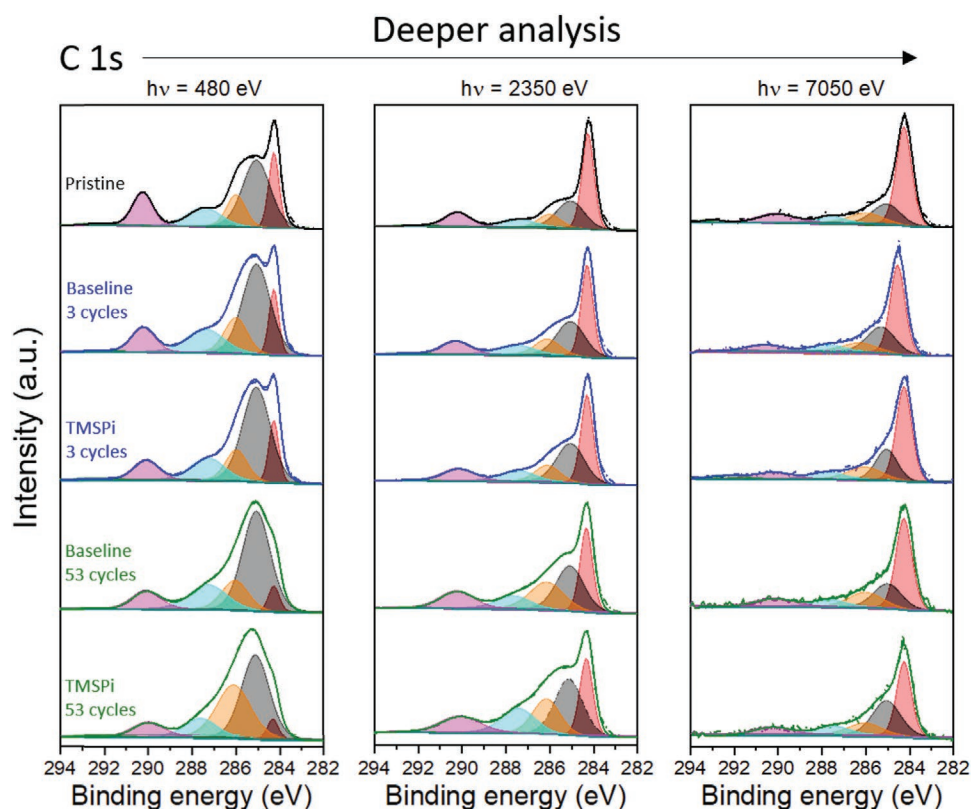


Figure 5. C 1s spectra of the pristine and harvested NMC811 electrodes taken from discharged cells after 3 and 53 cycles with the baseline and 2 wt% TMSPi electrolytes, respectively. Evolution as function of the analysis depth.

are presented in Figure S8 (Supporting Information). The NMC811 electrode consists of $\approx 3 \mu\text{m}$ spherical secondary particles, composed of $\approx 500 \text{ nm}$ primary particles, which were homogeneously distributed in the electrode. In general, the basic morphology of NMC811 particles are well preserved after cycling with both electrolytes. While there is almost no apparent change to NMC811 particles after 53 cycles with the baseline electrolyte, the surface of the electrode cycled with 2 wt% TMSPi was found to be covered by a layer, most likely by a compact CEI passivation film. The formed surface film originating from TMSPi is thought to prevent the potential occurrence of metal dissolution of NMC811 due to corrosion by HF, which forms due to the hydrolysis of LiPF_6 , and alleviate side reactions of the electrolyte at high cut-off voltage.^[24] As a result, a lower interfacial impedance, reduced polarization and high CE can be ascribed to the contribution from the benign CEI at the interface of NMC811/electrolyte by adding TMSPi.

To understand and compare the influence of the TMSPi additive on the surface chemistry of NMC811 electrodes after cycling, the nature of the CEI formed with the two electrolytes was characterized by synchrotron-based XPS. **Figures 5 and 6** show the C 1s, O 1s, and P 2p spectra of NMC811 electrodes harvested from the NMC811/Si-Gr full cells after 3 formation cycles and 53 cycles with the baseline and 2 wt% TMSPi electrolytes. At first observation, it is clear from the spectra that a CEI layer is built up during cycling. This can be seen from the decreased intensity of the peaks originating from the bulk material, such as C=C peaks in the C 1s spectra (Figure 5) and

the M–O peaks in the O 1s spectra (Figure 6). The CEI layer formed with TMSPi electrolyte seems to be a little thicker compared with the corresponding CEI formed with the baseline electrolyte. This suggests that the oxidation products of TMSPi contributed to build up the CEI and slightly increased its thickness, which is consistent with the observation from SEM as discussed above.

In detail, the C 1s spectra contains multiple components for the pristine electrode, from the $\text{CF}_2\text{-CH}_2$ ($\approx 290.2 \text{ eV}$) and $\text{CH}_2\text{-CF}_2$ ($\approx 286.0 \text{ eV}$) groups of the binder polyvinylidene difluoride (PVdF), respectively, and an additional minor peak at $\approx 292.5 \text{ eV}$, corresponding to CF_3 moiety, related to copolymers of PVdF.^[52] The component at $\approx 287.5 \text{ eV}$ is assigned to O–C–O/C=O species from carbon black.^[53] The peak at $\approx 284.7 \text{ eV}$ results from the C–C/C–H groups and the feature at 284.2 eV can be assigned to the sp^2 -hybridized C=C bond from carbon black. For the cycled electrodes, the C=C peak is visible at the surface region after 3 formation cycles, while its intensity decreases to be reflected by the shoulder at the same position after 53 cycles for both electrolytes. It reveals that the formed CEI is thinner at the beginning of the formation process, after which the thickness increases during cycling. The decomposition products of EC-DEC (C–O, C=O/O–C=O, carbonate) generated on the electrode surface are overlapping heavily with peaks from carbon black and PVdF as described above.

The O 1s spectra display three peaks at ≈ 529.0 , ≈ 531.5 , and $\approx 533.5 \text{ eV}$, which are attributed to the transition metal oxide (M–O) in NMC811, chemically formed C=O species, such as

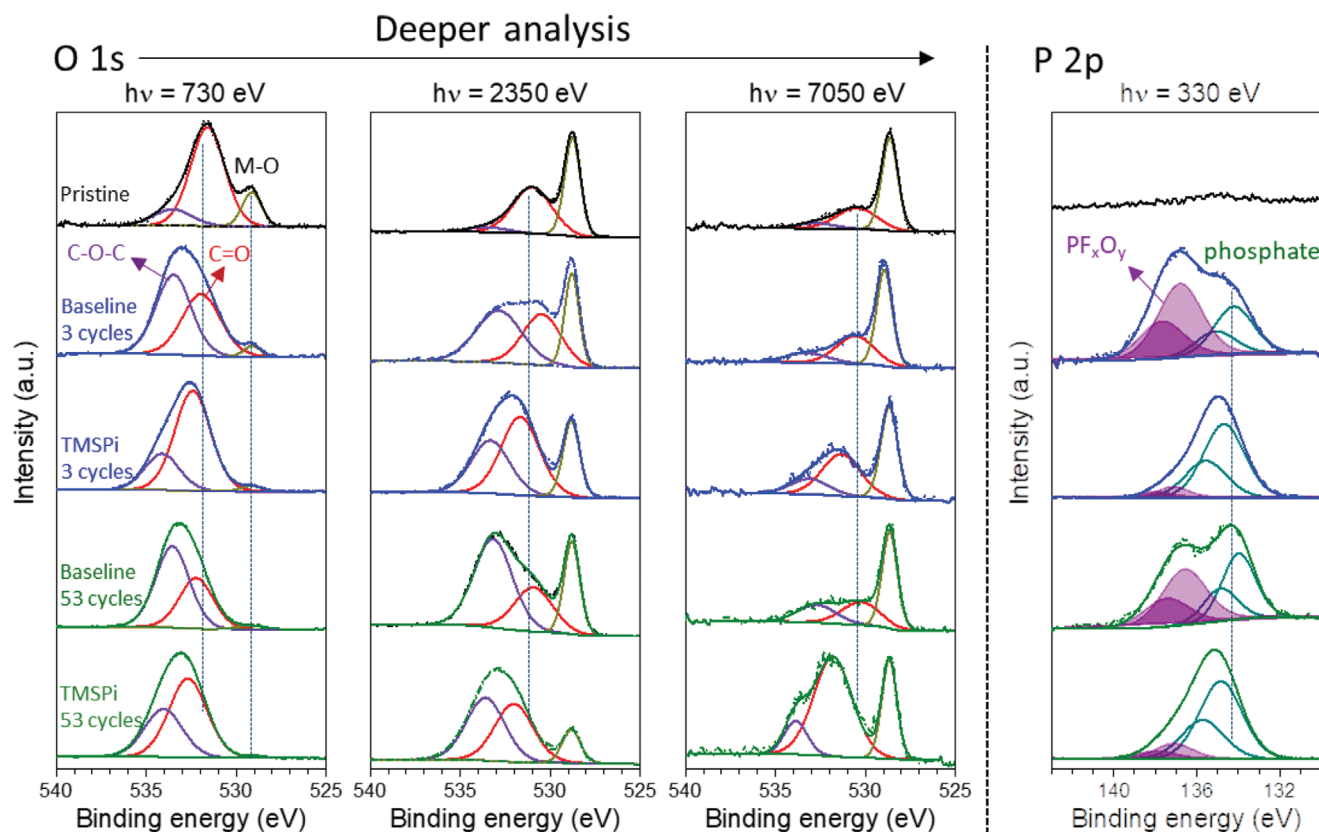


Figure 6. O 1s and P 2p spectra of the pristine and harvested NMC811 electrodes taken from discharged cells after 3 and 53 cycles with the baseline and 2 wt% TMSPi electrolytes, respectively. Evolution as function of the analysis depth.

Li_2CO_3 due to the reactive surface of NMC811, and the oxidized conductive carbon (C–O–C). The M–O feature is more sensitive with increased excitation energy, indicating that lithium carbonate residues formed on the surface of the NMC811 electrode. It is found that both C–O–C and C=O peaks shift to higher binding energy (≈ 0.5 eV) for all the cycled NMC811 electrodes with TMSPi electrolyte, as a result of P–O species existing in the CEI due to TMSPi decomposition. In general, the C–O component (≈ 533.5 eV) is the most pronounced in the O1s spectra with the baseline electrolyte due to the severe electrochemical decomposition of the solvent and salt. By comparison, an increased intensity for the C=O component from alkyl carbonates is dominant across the different depths with the TMSPi electrolyte, indicating the CEI-modifying ability of TMSPi.

As expected, no peaks are present in the P 2p spectra of the pristine NMC811 electrode in Figure 6. In the P 2p spectra for cycled electrodes, different environments each consisting of two spin orbit split peaks at a distance of 0.84 eV can be identified.^[54] We can clearly determine that degradation of LiPF_6 salt occurs upon cycling because all cycled samples show the presence of different P 2p environments. The lower binding energy feature at ≈ 134.5 eV corresponds well to the phosphate compounds (P–O/P=O).^[55] The higher binding energy feature of 136.8 eV originates from the decomposition products $\text{Li}_x\text{PO}_y\text{F}_z$. The phosphate species are enriched in the CEI with the TMSPi electrolyte, inferred from the ratios of the phosphate to PF_xO_y . This is likely a result of contributions from P–O bonds

in TMSPi and/or corresponding oxidative products. In other words, there is a significant increase on the PO_xF_y component with the baseline electrolyte, which is identified as common decomposition products of LiPF_6 , suggesting TMSPi could effectively suppress the LiPF_6 decomposition. It confirms that the TMSPi participates in the formation of the CEI from the formation step, and this phosphate-enrich CEI is robust and can stabilize the chemical compositions.

Spectra for additional core levels can be found in Figure S9 (Supporting Information). For the pristine NMC811 electrode, the peak at ≈ 687.5 eV in the spectra of F 1s is assigned to the C–F bond in PVdF binder. Additionally, there is a small shoulder at ≈ 684.5 eV, attributed to presence of LiF on the surface, which possibly arises from the parasitic dehydrofluorination of PVdF.^[23,56] For the cycled electrodes, the LiF peak becomes more visible along with a PO_xF_y component, which are identified as common decomposition products of LiPF_6 . In general, no obvious difference at the surface from both electrolytes can be observed from the F 1s spectra. For Li 1s spectra, the peak at ≈ 55.2 eV can be assigned to Li_2CO_3 and a small shoulder peak at ≈ 53.6 eV, is attributed to the Li–M in NMC811. After cycling, the Li–M peaks diminished and an increase of LiF/ $\text{Li}_x\text{PO}_y\text{F}_z$ is seen, consistent with components from common electrolyte degradation products. However, there is no evident change in the relative intensity of LiF/ $\text{Li}_x\text{PO}_y\text{F}_z$ species after long cycling with the TMSPi electrolyte, while a large increase is obtained with the baseline electrolyte. This reveals

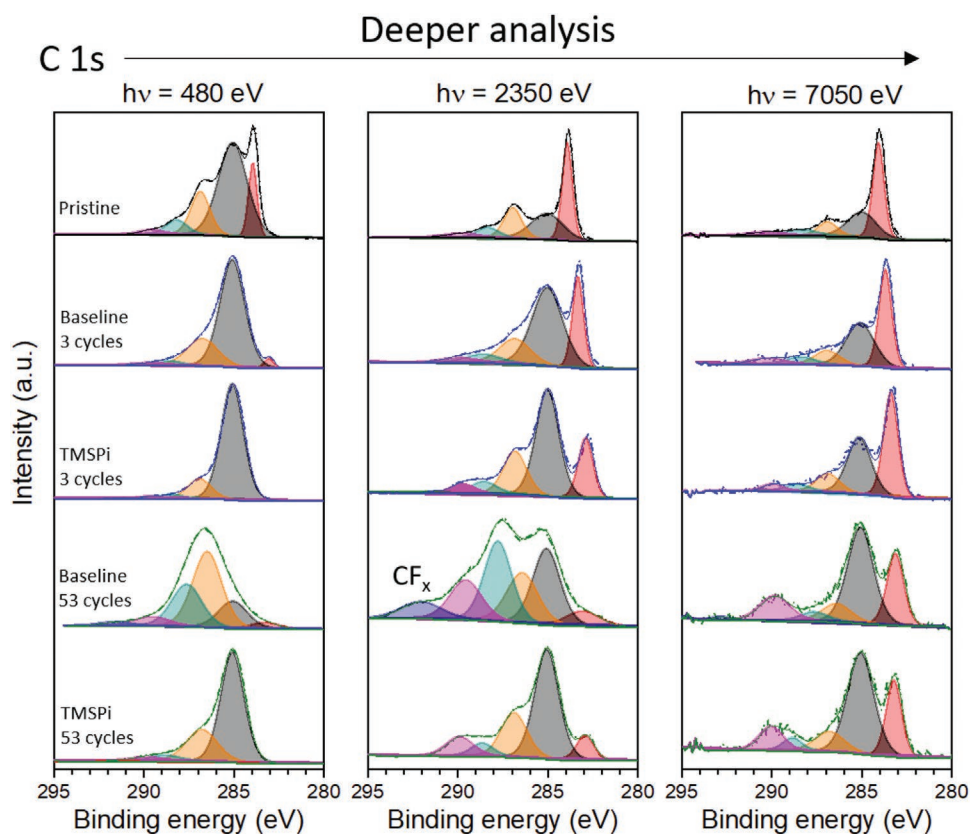


Figure 7. C 1s spectra of the pristine and harvested Si-Gr electrodes taken from discharged cells after 3 and 53 cycles in the baseline and 2 wt% TMSPi electrolytes, respectively. Evolution as function of the analysis depth.

that the TMSPi-derived CEI can effectively prevent the electrolyte degradation on the NMC811 electrode.

2.3.2. Surface Chemistry on the Si-Gr Anode

The morphology of the Si-Gr electrodes with the two electrolytes before and after cycling was also investigated by SEM (Figure S10, Supporting Information). There are significant differences between the surface morphologies of the pristine and cycled Si-Gr electrodes with the baseline electrolyte and the TMSPi electrolyte. The Si-Gr electrode cycled with the baseline electrolyte shows island-like particles of a few micrometers, which is mainly caused by the severe electrochemical decomposition of electrolyte and possible pulverization of Si active material because of enormous volume expansion (lithiation)/contraction (delithiation). However, the cycled electrode with TMSPi electrolyte displays a relatively uniform surface that seems to be covered by a dense and uniform SEI layer, although minor cracks on the surface can be observed at high magnification. This result strongly suggests that TMSPi improves the interfacial stability of Si-Gr anode.

Figure 7 presents the C 1s spectra measured with photon energies of 480, 2350, and 7050 eV for the Si-Gr electrodes cycled in the two electrolytes after 3 formation and 53 cycles, respectively, with respect to the pristine electrode. The dominant detected component at the surface region of pristine

Si-Gr electrode at 285.0 eV is attributed to C-C/C-H bonds from adventitious carbon and SBR and CMC binders. The components at ≈ 284.0 eV can be assigned to the graphitic carbon C=C bond from graphite and carbon black. The peaks at 286.8, 288.2, and 289.6 eV correspond to C-O, O-C-O, and OCO₂ bonds, respectively, from particle surface species or from graphite.^[57,58] In the near-surface (2350 eV) and bulk-sensitive (7050 eV) regions, the C=C peak becomes more visible with increased relative intensity.

The typical SEI components, such as C-C, C-O, O-C-O/C=O, and OCO₂-based compounds formed by EC reduction, can be observed in the C 1s spectra for cycled Si-Gr electrodes.^[27,59] For harvested Si-Gr electrodes after formation cycles with TMSPi electrolyte, the C=C peak is no longer visible at the surface for the 480 eV measurement and has relatively lower intensity at the near-surface region than that with the baseline electrolyte, indicating that an SEI film has already formed on the surface of Si-Gr anode. A similar trend is obtained for both electrolytes after 53 cycles. This result agrees well with SEM observations. The bulk-sensitive regions in the 7050 eV measurements exhibit a more pronounced C=C peak and similar chemical components for both harvested electrodes. The most substantial changes in elemental compositions is obtained after 53 cycles with the baseline electrolyte, where the C-O and O-C-O/C=O peaks become more dominant and have higher relative intensity, compared with that after 3 formation cycles. This means that the formed SEI

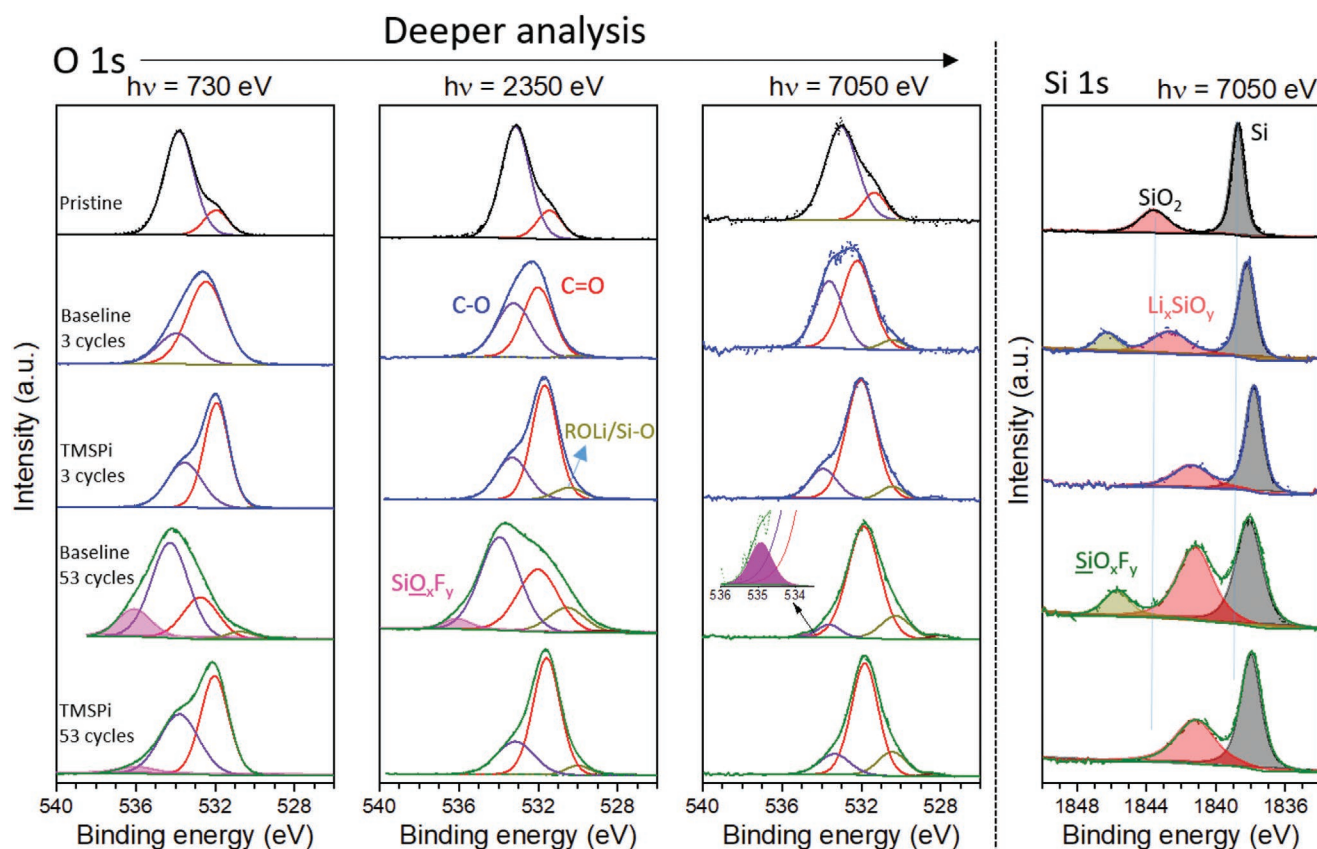


Figure 8. O 1s and Si 1s spectra of the spectra of the pristine and harvested Si-Gr electrodes taken from discharged cells after 3 and 53 cycles with the baseline and 2 wt% TMSPi electrolytes, respectively. Evolution as function of the analysis depth for O 1s.

with the baseline electrolyte continues to change with cycling. Moreover, a new peak at ≈ 292.0 eV corresponding to C-F species emerged, which may be caused by the migration of decomposed species of PVDF binder from the cathode. This “crosstalk” phenomenon between cathode and anode was also observed by Leanza, et al recently.^[43] It can also be seen that the chemical composition of the SEI formed in the baseline electrolyte greatly varies with different depths. However, the C 1s spectrum of the harvested electrode with TMSPi shows no clear change. It reveals that the TMSPi-derived SEI film is robust and stable, assuring good cycling stability of the Si-Gr electrode.

The O 1s spectra of the harvested Si-Gr electrodes with three different probing depths are also analyzed as shown in Figure 8. Compared with the pristine electrode, which has a higher amount of ether-oxygen (≈ 533.8 eV) than carbonyl oxygen (≈ 532.1 eV), the spectra are dominated by a carbonyl signal at ≈ 532 eV for both harvested electrodes after the formation cycles. This is attributed to the carbonate and carboxylate components formed from the reduction of organic solvents in the electrolytes. For the cycled Si-Gr electrodes after 53 cycles, the SEI formed in the TMSPi electrolyte has overall evenly distributed O-species at all depths. However, the surface of the SEI formed in the baseline electrolyte contains more ether-oxygen species, while the inner part at the near-surface region has increased carbonate species. It is also noticed that a component at ≈ 536.0 eV is present for the baseline electrolyte with a higher intensity close to the surface. This can be assigned to

the fluorinated species SiO_xF_y , due to the HF acidic attack on the electrode after long cycling. However, only a small amount of SiO_xF_y is detected at the surface of the cycled electrode with TMSPi electrolyte and this component is absent at the near-surface and bulk regions, suggesting the TMSPi-derived SEI film could effectively protect Si particles from the fluoridation reactions after long cycling periods.

The fluoridation process at the bulk-sensitive region is further explored by analyzing Si 1s spectra in the 7050 eV measurements as displayed in Figure 8. For the pristine Si-Gr electrode, a thin SiO_2 layer (≈ 1843.5 eV) is evident in addition to bulk silicon (≈ 1838.6 eV). These species are also evident in Si 2p spectra in Figure S11 (Supporting Information), with SiO_2/Si area ratio reduced due to the increased analysis depth on the pristine electrode. After cycling with the baseline electrolyte, a new peak at ≈ 1846.0 eV emerged at high binding energy, which can be assigned to the SiO_xF_y component. The Si2p spectra demonstrate that small amounts of fluorinated species already exist at both surface and near-surface regions in the baseline electrolyte after the formation cycles. By comparison, no fluorinated species is detected at any depth with the TMSPi electrolyte. Moreover, lithium silicate Li_xSiO_y formed by lithiation of SiO_2 , is present at the surface of Si particles, characterized by the peak at ≈ 1841.5 eV in the Si 1s spectra.^[28] Upon cycling with the baseline electrolyte, a significant increase of the amount of fluorinated and lithiated silicate can clearly be seen, but a relatively stable composition of Si-based species remained in the TMSPi electrolyte.

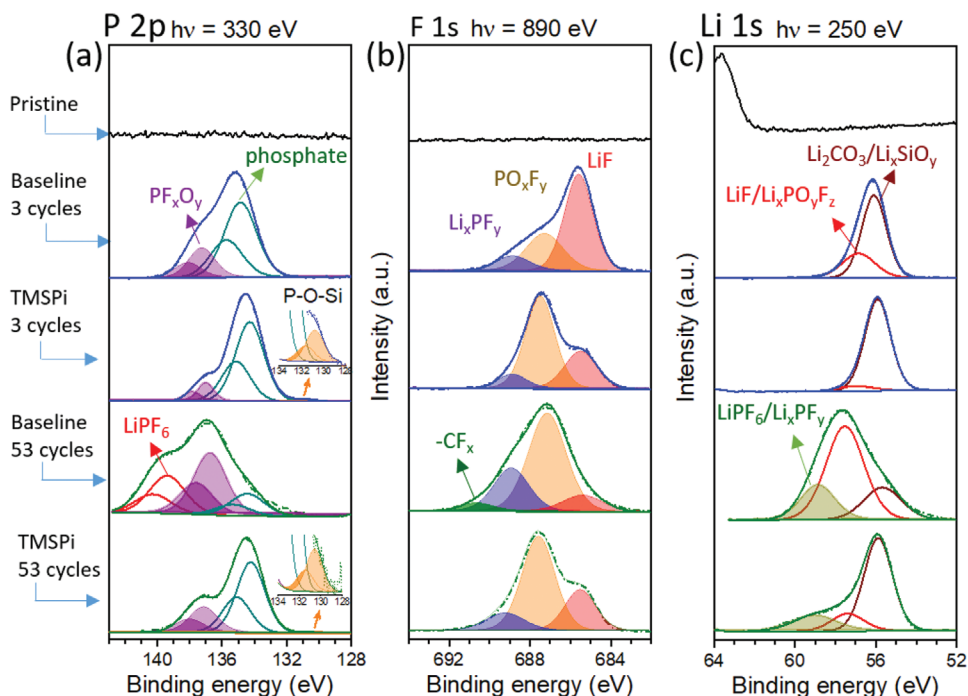


Figure 9. a) P 2p, b) F 1s, and c) Li 1s spectra of the pristine and harvested Si–Gr electrodes taken from the discharged cells after 3 and 53 cycles in the baseline and 2 wt% TMSPi electrolytes, respectively. The kinetic energy of the photoelectrons was kept the same, 200 eV, to obtain the same probing depth for these elements at the surface region.

The surface species formed by reduction of the electrolyte can provide additional information. **Figure 9** shows the P 2p, F 1s and Li 1s spectra of the pristine and harvested Si–Gr electrodes after cycling with two electrolytes. In the P 2p spectra for cycled electrodes, two spin orbit split peaks at a distance of 0.84 eV for each different environment can be identified.^[54] It is also seen that this degradation continues upon cycling since the P 2p signal intensity (PF_xO_y species) consistently increases up to 53 cycles. Notably, a higher binding energy feature appears at ≈ 139 eV, which is close to the value for the LiPF_6 residue and this peak shift can be caused by the poor conductive character of the large amounts of decomposition compounds on the surface.^[60] It suggests that some LiPF_6 salt cannot be completely rinsed off by dimethyl carbonate (DMC), with some remaining in the SEI or trapped in pores after long cycling because of the severe solvent decomposition and fluorination with the baseline electrolyte. Importantly, a unique peak at ≈ 130.8 eV generated with the TMSPi electrolyte, which can be assigned to P–O–Si species, originating from TMSPi and/or its decomposition products by P–O and Si–O bond cleavages.^[38] This also supports that TMSPi participated in the formation of the SEI layer at the Si–Gr electrode and the TMSPi-derived SEI can stabilize the interfacial stability and effectively mitigate the electrolyte degradation because no significant change of P 2p environment is detected after long cycling.

In F 1s spectra of all the cycled electrodes (Figure 9 and Figure S12a, Supporting Information), there are at least three peaks at ≈ 685.5 , 687.2, and 688.8 eV, assigned to the formation of LiF, PF_yO_x , and LiPF_x species, respectively, due to the chemical decomposition of LiPF_6 as well as subsequent hydrolysis.^[61] Particularly for the electrode at 53 cycles with the

baseline electrolyte, fluoro-organic species (CF_x) is detected at ≈ 690.5 eV in the SEI. The determined position is comparable to typical values for $\text{CF}_2/\text{CF}_3/-(\text{CF}_2)_n-$ groups, previously reported in the literature (≈ 690 eV).^[62,63] As discussed above, this CF_x species was also observed in the C 1s spectrum. In this context, it is believed that CF_x species is associated with the “crosstalk” due to the oxidative decomposition of PVdF binder from the cathode to anode. By contrast, no CF_x peak is observed after long cycling with TMSPi additive, indicating the TMSPi-derived CEI on the cathode can effectively suppress the PVdF degradation and “crosstalk.” Li 1s spectra additionally indicate more F-containing species at the surface of cycled electrodes with the baseline electrolyte as seen from Figure 9c and Figure S12b (Supporting Information). Higher amounts of Li salts, like Li_xPF_y and LiF (≈ 58.8 and ≈ 57.2 eV) are observed with the baseline electrolyte, while carboxylate species at ≈ 56.0 eV, such as Li_2CO_3 , is the dominant composition for the TMSPi electrolyte.

Overall, a significant difference in elemental distribution can be confirmed from the overview spectra presented in Figure S13 (Supporting Information), which were measured with a photon energy of 2350 eV for the cycled Si–Gr electrodes. The baseline electrolyte generated more fluorinated species due to severe electrolyte decomposition and LiPF_6 hydrolysis by traces of water.^[61,64] However, the TMSPi-containing electrolyte facilitated the formation of O-rich species on the surface derived from TMSPi and/or its decomposition products. In general, P, F, O-based species are not homogeneously distributed across the SEI, supported by the depth profiling analysis. By comparison, the variation of these species with depth when using the TMSPi electrolyte is much smaller.

It can be seen that SEM and XPS depth-profiling studies revealed distinct chemical compositions of the cycled NMC811 and Si-Gr electrodes depending on the use of TMSPi. It is demonstrated that the TMSPi additive can sufficiently limit the continuous change of CEI and SEI chemistries resulting from the decomposition of organic solvents and achieve good cycling stability and high Coulombic efficiency. These results reveal that the use of TMSPi is beneficial to improve the interfacial stability during charge/discharge processes for NMC811/Si-Gr full cells.

3. Conclusion

In this study, the behaviors of the high energy density cells containing NMC811 cathode and Si-Gr anode cycled in the voltage range of 2.7–4.4 V have been presented. The influence of 2 wt% TMSPi additive in the baseline electrolyte (1 M LiPF₆ in EC:DEC) on the electrochemical performance of the NMC811/Si-Gr full cells was investigated in pouch cells by performing different measurements to determine electrochemical response, structure, surface morphology and depth-dependent composition. TMSPi additive in the NMC811/Si-Gr full cells increased the discharge capacity, slowed down the increase of overpotential and surface impedance with cycling, increased the Coulombic efficiency, and improved cycling stability.

In particular, structural analysis of NMC811/Li half cells using operando XRD measurements, confirmed that the addition of TMSPi could break down the formed adventitious Li₂CO₃ surface layer due to the reactive surface of NMC811 to allow for a solid-solution evolution instead of a “two-phase” reaction mechanism. Moreover, the morphological and compositional differences of the CEI and SEI on their respective electrodes were investigated by SEM and synchrotron-based XPS for depth profiling. The robust CEI and SEI films at the electrode/electrolyte interfaces can effectively stabilize NMC811 cathode and Si-Gr anode during cycling. The formed CEI with TMSPi on the NMC811 cathodes displayed an increased amount of alkyl carbonates/carboxylates at different depths, with a decreased amount of PO_xF_y species. Moreover, this TMSPi-derived CEI on the cathode can effectively suppress the PVDF degradation and the cathode to anode “crosstalk” of the migration of the decomposed –CF_x species. TMSPi and/or its decomposition products participated in forming an initial SEI that contains distinctive species (P–O–Si-based compounds), which maintains the interfacial stability and prevent extensive SEI reformation with ongoing cycling of the Si-Gr anode. Our observations from the surface analysis also confirm that TMSPi can serve as an HF scavenger, avoiding fluorination of Si particles. It is also believed the HF elimination from electrolyte and compact TMSPi-derived CEI film are beneficial to the electrochemical stability of NMC811. Hence, a novel finding is suggested that TMSPi could serve as not only a HF scavenger but also a potential Li-residue scavenger. Overall, it is shown that TMSPi and/or its decomposition products participated in the formation of stable and robust CEI and SEI layers, responsible for the improved cycling stability of the NMC811/Si-Gr full cells, as illustrated in Figure 10.

This work provides a valuable understanding of the effects of TMSPi on NMC811 cathode, Si-Gr anode and their coupled

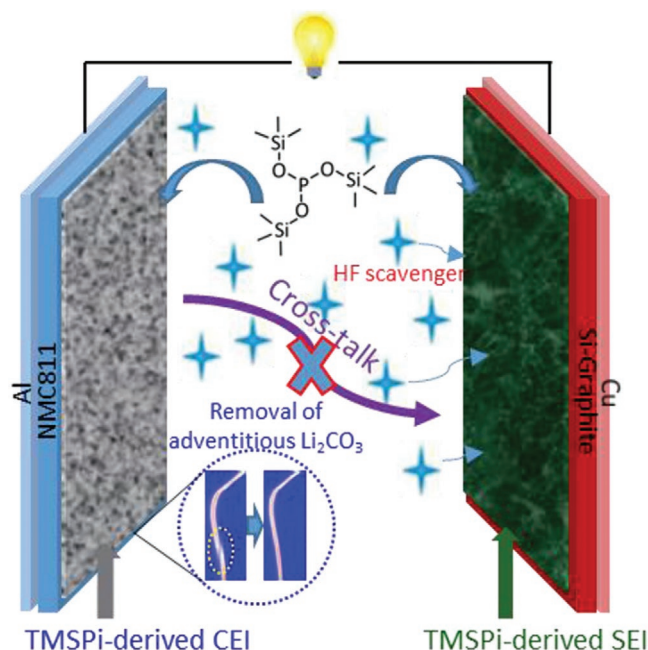


Figure 10. Schematic illustration of the working mechanism of the TMSPi additive in the NMC811/Si-Gr full cell.

full cells and offers new insight. This paves the way for further development and optimization of suitable electrolyte formulations used in configurations containing both Ni-rich cathodes and Si-based anodes for high energy-density LIBs.

4. Experimental Section

Electrode and Electrolyte Preparation: The NMC811 electrode was prepared by mixing a slurry containing 90 wt% NMC811 powder (Customcells Itzehoe GmbH), 5 wt% of super C65 (Imerys) and 5 wt% PVDF (Solvay) in *N*-methyl-2-pyrrolidone (NMP) using a MM 400 mixer mill (Retsch). The obtained slurry was cast on Al foil, using a doctor blade, predried at 60 °C for 3 h and then at 120 °C for 12 h under vacuum. The active-material loading of the as-prepared electrode was ≈10 mg cm⁻², corresponding to an areal capacity of ≈1.9 mAh cm⁻² between 3 and 4.5 V versus Li/Li⁺.

The Si-Gr electrode sheets consisting of 77.5 wt% graphite and 12.5 wt% Si with styrene butadiene rubber (SBR) and sodium carboxymethylcellulose (Na-CMC) as binder, was purchased from Customcells Itzehoe GmbH (Germany). The nominal areal capacity of the Si-Gr electrode was 2.2 ± 0.5 mAh cm⁻², as determined by the capacity of the cathode in order to fulfill a suitable anode/cathode capacity balancing. For the full cell investigation, the capacity ratio of the NMC811 cathode and the Si-Gr anode was set to 1:1.15 to avoid the lithium plating on the anode.

The influence of the electrolyte additive TMSPi on the electrochemical behaviors of the NMC811/Si-Gr cells was evaluated within the benchmark electrolyte 1 M LiPF₆ in a mixture of ethylene carbonate/diethylene carbonate (EC/DEC 1:1 by volume, Solvionic, purity: 99.9%), which was defined as baseline electrolyte in this study. The electrolyte with additive was formulated by adding 2 wt% of tris(trimethylsilyl) phosphite (TMSPi, Sigma-Aldrich; purity: 95%) to the baseline electrolyte. The electrolyte preparation and storage as well as the cell assemble were carried out in an Ar-filled glovebox.

Cell Preparation and Electrochemical Characterization: Single layer pouch cells were assembled in an Ar-filled glovebox. Full cells were

composed of NMC811 as cathode, Si–Gr as anode and Celgard 2325 as separator. NMC811/Li half cells consisting of NMC811 electrode, Li metal, and Celgard 2325 were used for the operando XRD measurements. Si–Gr/Li half cells consisting of Si–Gr electrode, Li metal, and Celgard 2325 were used for the cyclic voltammetry experiments.

The electrochemical charge/discharge cycling of the assembled cells was performed on an Arbin battery analysis system at room temperature. The NMC811/Si–Gr full cells were charged/discharged between 2.7 and 4.4 V with three formation cycles at 0.1 C via a constant current and constant voltage (CCCV) mode. The constant voltage charge/discharge step at 4.4/2.7 V after the constant current charge/discharge process was applied until the current dropped below/rose above 0.01/–0.01 C, respectively. A specific current of 200 mA g^{–1} is defined as 1 C. Afterward, the full cells were charged/discharged at 0.5 C using the constant current (CC) mode. The calculation of the capacity retention after certain cycles is based on the discharge capacity of the fourth cycle after the formation process. For the investigation of high rate capability, the cells were discharged at different current densities corresponding to 0.1, 0.2, 0.5, 1, 2, 5 C with a constant charge rate of 0.2 C after the initial cycles at 0.1 C between 2.7 and 4.4 V. The NMC811/Li and Si–Gr/Li half cells were examined via constant current charge/discharge mode. Storage tests were performed after the first charging of the NMC811/Si–Gr full cell to 4.4 V, and the open-circuit voltage (OCV) was recorded at room temperature for 500 hours.

LSV was carried out on a three-electrode cell using a Pt disc (8 mm in diameter) as working electrode with metallic lithium as counter and reference electrodes using a scan rate of 1 mV s^{–1}. CV of the Si–Gr/Li cells was performed with a scan rate of 0.05 mV s^{–1} within a voltage range of 0.01–1 V. EIS measurements of NMC811/Si–Gr full cells were carried out with the frequency range set from 100 kHz to 10 mHz with a 10 mV amplitude perturbation. All LSV, CV, and EIS measurements were conducted on a VMP instrument (Bio-Logic). All the electrochemical characterizations were performed at room temperature.

Structural and Morphological Characterization: XRD data of the pristine NMC811 powder was collected between 10° and 90° with a step size of 0.019° and a 4 s time per step on a Bruker D8 Advance diffractometer (40 kV, 40 mA) using Cu-K α radiation. The operando XRD measurements were conducted in transmission mode through pouch-type cells with two different electrolytes on a STOE STADI P diffractometer equipped with a Ge monochromator (Cu K α_1 radiation).^[65] The pouch cell was galvanostatically charged and discharged at 0.1 C in a voltage range of 3–4.5 V versus Li/Li⁺ with a SP-150 potentiostat (Bio-Logic). At the same time, the diffraction data was collected using a Mythen 1K strip detector operated in sweeping mode to cover a 2 θ range from 15° to 51° with a step size of 0.495 and 5 s time per step (\approx 5 patterns h^{–1}). Rietveld refinements of the X-ray data were performed using the Topas (Version 6.0) software based on the crystallographic information obtained from the Inorganic Crystal Structure Database (ICSD, #184697).

SEM (Zeiss Merlin) images were taken at an operating voltage of 3 kV using an in-lense detector to study the morphology of both electrodes after washing with DMC.

Energy-Tuned XPS Analysis: Before all XPS measurements, the cells were disassembled inside an Ar-filled glovebox, and the electrodes were carefully washed with DMC to reduce the amount of electrolyte residue. The samples were mounted on a copper plate using copper tape and loaded onto the end-station at the synchrotron. Soft-/Hard-XPS measurements were conducted on the I09 beamline at Diamond Light Source synchrotron facility (Oxfordshire, UK). For soft XPS characterization, all XPS core levels were measured with the same kinetic energy of 200 eV for the photoelectrons in order to obtain the same probing depth, which was realized by varying the photon energy of the X-rays accordingly. For hard XPS characterization, two different photon energies were used, 2350 and 7050 eV, corresponding to the first and third order X-ray from the Si (111) double-crystal monochromator. No charge neutralizer was utilized during the measurements. The spectra were recorded by a hemispherical Scienta EW4000 analyzer with a pass energy of 50 eV for soft X-rays, 70 eV for 2.35 keV hard X-rays, and 200 eV for 7.05 keV hard X-rays. All of the obtained XPS spectra were

processed with CasaXPS software and calibrated by the hydrocarbon (C–H) signal at the binding energy of 285 eV after curve fitting. In the XPS figures, spectra were normalized to show the relative intensities of the different components. Approximate probing depths as shown in Table S1 (Supporting Information) was estimated using the IMFP values of polyethylene derived from the NIST database.^[66,67] These values can be considered as an upper limit for the probing depths since they are mostly representative of the low-density surface layer studied here, while for the denser inorganic materials, smaller probing depths would be expected.

Supporting Information

Supporting Information is available from the Wiley Online Library or from the author.

Acknowledgements

The financial support for this work was granted through the LIBchallenge project funded by Swedish Energy Agency (Energimyndigheten). The authors also gratefully acknowledge funding from the Strategic Research Area StandUp for Energy. A.S.M. is grateful for the funding received from the Swedish Foundation for Strategic Research (SSF) within the Swedish national graduate school in neutron scattering (SwedNess). XPS work was carried out with the support of the Diamond Light Source, instrument I09 (proposal SI23159-1). The research was also supported by the project CALIPSOplus under Grant Agreement 730872 from the EU Framework Programme for Research and Innovation HORIZON 2020.

Conflict of Interest

The authors declare no conflict of interest.

Keywords

additives, lithium-ion batteries, NMC811/Si–graphite full cells, operando XRD

Received: February 18, 2020

Revised: May 4, 2020

Published online: June 8, 2020

- [1] M. Li, J. Lu, Z. W. Chen, K. Amine, *Adv. Mater.* **2018**, *30*, 1800561.
- [2] J. Kim, H. Lee, H. Cha, M. Yoon, M. Park, J. Cho, *Adv. Energy Mater.* **2018**, *8*, 1702028.
- [3] E. Björklund, M. Göttlinger, K. Edström, D. Brandell, R. Younesi, *ChemElectroChem* **2019**, *6*, 3429.
- [4] R. Schmuck, R. Wagner, G. Horpel, T. Placke, M. Winter, *Nat. Energy* **2018**, *3*, 267.
- [5] S. T. Myung, F. Maglia, K. J. Park, C. S. Yoon, P. Lamp, S. J. Kim, Y. K. Sun, *ACS Energy Lett.* **2017**, *2*, 196.
- [6] H. J. Noh, S. Youn, C. S. Yoon, Y. K. Sun, *J. Power Sources* **2013**, *233*, 121.
- [7] A. Manthiram, B. H. Song, W. D. Li, *Energy Storage Mater.* **2017**, *6*, 125.
- [8] H. Maleki Kheimeh Sari, X. Li, *Adv. Energy Mater.* **2019**, *9*, 1901597.
- [9] M. S. Whittingham, *Chem. Rev.* **2014**, *114*, 11414.
- [10] U. Kasavajula, C. S. Wang, A. J. Appleby, *J. Power Sources* **2007**, *163*, 1003.

- [11] K. Feng, M. Li, W. W. Liu, A. G. Kashkooli, X. C. Xiao, M. Cai, Z. W. Chen, *Small* **2018**, *14*, 1702737.
- [12] H. Kim, E. J. Lee, Y. K. Sun, *Mater. Today* **2014**, *17*, 285.
- [13] D. Larcher, S. Beattie, M. Morcrette, K. Edstroem, J. C. Jumas, J. M. Tarascon, *J. Mater. Chem.* **2007**, *17*, 3759.
- [14] R. A. Huggins, *J. Power Sources* **1999**, *81*, 13.
- [15] S. Chae, S.-H. Choi, N. Kim, J. Sung, J. Cho, *Angew. Chem., Int. Ed.* **2020**, *59*, 110.
- [16] M. Otero, C. Heim, E. P. M. Leiva, N. Wagner, A. Friedrich, *Sci. Rep.* **2018**, *8*, 15851.
- [17] N. Dimov, S. Kugino, A. Yoshio, *J. Power Sources* **2004**, *136*, 108.
- [18] K. Kalaga, I. A. Shkrob, R. T. Haasch, C. Peebles, J. Bareno, D. P. Abraham, *J. Phys. Chem. C* **2017**, *121*, 23333.
- [19] Z. Yi, W. W. Wang, Y. Qian, X. Y. Liu, N. Lin, Y. T. Qian, *ACS Sustainable Chem. Eng.* **2018**, *6*, 14230.
- [20] X. L. Li, P. F. Yan, X. C. Xiao, J. H. Woo, C. M. Wang, J. Liua, J. G. Zhang, *Energy Environ. Sci.* **2017**, *10*, 1427.
- [21] C. H. Yim, F. M. Courtel, Y. Abu-Lebdeh, *J. Mater. Chem. A* **2013**, *1*, 8234.
- [22] J. Bareno, I. A. Shkrob, J. A. Gilbert, M. Klett, D. P. Abraham, *J. Phys. Chem. C* **2017**, *121*, 20640.
- [23] K. Beltrop, S. Klein, R. Nolle, A. Wilken, J. J. Lee, T. K. J. Koster, J. Reiter, L. Tao, C. D. Liang, M. Winter, X. Qi, T. Placke, *Chem. Mater.* **2018**, *30*, 2726.
- [24] H. J. Zhao, X. Q. Yu, J. D. Li, B. Li, H. Y. Shao, L. Li, Y. H. Deng, *J. Mater. Chem. A* **2019**, *7*, 8700.
- [25] C.-G. Shi, C.-H. Shen, X.-X. Peng, C.-X. Luo, L.-F. Shen, W.-J. Sheng, J.-J. Fan, Q. Wang, S.-J. Zhang, B.-B. Xu, J.-J. Xian, Y.-M. Wei, L. Huang, J.-T. Li, S.-G. Sun, *Nano Energy* **2019**, *65*.
- [26] J. Y. Li, W. D. Li, Y. You, A. Manthiram, *Adv. Energy Mater.* **2018**, *8*, 1801957.
- [27] B. Philippe, M. Hahlin, K. Edstrom, T. Gustafsson, H. Siegbahn, H. Rensmo, *J. Electrochem. Soc.* **2016**, *163*, A178.
- [28] B. Philippe, R. Dedryvere, J. Allouche, F. Lindgren, M. Gorgoi, H. Rensmo, D. Gonbeau, K. Edstrom, *Chem. Mater.* **2012**, *24*, 1107.
- [29] F. Lindgren, C. Xu, L. Niedzicki, M. Marcinek, T. Gustafsson, F. Bjorefors, K. Edstrom, R. Younesi, *ACS Appl. Mater. Interfaces* **2016**, *8*, 15758.
- [30] C. Xu, F. Lindgren, B. Philippe, M. Gorgoi, F. Bjorefors, K. Edstrom, T. Gustafsson, *Chem. Mater.* **2015**, *27*, 2591.
- [31] T. Jaumann, J. Balach, U. Langklotz, V. Sauchuk, M. Fritsch, A. Michaelis, V. Teltevschij, D. Mikhailova, S. Oswald, M. Klose, G. Stephani, R. Hauser, J. Eckert, L. Giebeler, *Energy Storage Mater.* **2017**, *6*, 26.
- [32] A. M. Haregewoin, A. S. Wotango, B.-J. Hwang, *Energy Environ. Sci.* **2016**, *9*, 1955.
- [33] X. Qi, L. Tao, H. Hahn, C. Schultz, D. R. Gallus, X. Cao, S. Nowak, S. Roser, J. Li, I. Cecik-Laskovic, B. R. Rad, M. Winter, *RSC Adv.* **2016**, *6*, 38342.
- [34] C. Peebles, R. Sahore, J. A. Gilbert, J. C. Garcia, A. Tornheim, J. Bareno, H. Iddir, C. Liao, D. P. Abraham, *J. Electrochem. Soc.* **2017**, *164*, A1579.
- [35] A. Tornheim, C. Peebles, J. A. Gilbert, R. Sahore, J. C. Garcia, J. Bareno, H. Iddir, C. Liao, D. P. Abraham, *J. Power Sources* **2017**, *365*, 201.
- [36] W. D. Qiu, J. Xia, L. P. Chen, J. R. Dahn, *J. Power Sources* **2016**, *318*, 228.
- [37] Y. K. Han, J. Yoo, T. Yim, *J. Mater. Chem. A* **2015**, *3*, 10900.
- [38] T. Yim, Y. K. Han, *ACS Appl. Mater. Interfaces* **2017**, *9*, 32851.
- [39] C. Peebles, J. Garcia, A. P. Tornheim, R. Sahore, J. Bareno, C. Liao, I. A. Shkrob, H. H. Iddir, D. P. Abraham, *J. Phys. Chem. C* **2018**, *122*, 9811.
- [40] S. W. Mai, M. Q. Xu, X. L. Liao, J. N. Hu, H. B. Lin, L. D. Xing, Y. P. Liao, X. P. Li, W. S. Li, *Electrochim. Acta* **2014**, *147*, 565.
- [41] Y. M. Song, J. G. Han, S. Park, K. T. Lee, N. S. Choi, *J. Mater. Chem. A* **2014**, *2*, 9506.
- [42] E. Bjorklund, D. Brandell, M. Hahlin, K. Edstrom, R. Younesi, *J. Electrochem. Soc.* **2017**, *164*, A3054.
- [43] D. Leanza, C. A. F. Vaz, G. Melinte, X. K. Mu, P. Novak, M. El Kazzi, *ACS Appl. Mater. Interfaces* **2019**, *11*, 6054.
- [44] J. Kasnatscheew, B. Streipert, S. Roser, R. Wagner, I. C. Laskovic, M. Winter, *Phys. Chem. Chem. Phys.* **2017**, *19*, 16078.
- [45] A. Grenier, H. Liu, K. M. Wiaderek, Z. W. Lebens-Higgins, O. J. Borkiewicz, L. F. J. Piper, P. J. Chupas, K. W. Chapman, *Chem. Mater.* **2017**, *29*, 7345.
- [46] P. Meister, H. P. Jia, J. Li, R. Kloepsch, M. Winter, T. Placke, *Chem. Mater.* **2016**, *28*, 7203.
- [47] Q. Q. Liu, L. Ma, C. Y. Du, J. R. Dahn, *Electrochim. Acta* **2018**, *263*, 237.
- [48] J. Li, L. E. Downie, L. Ma, W. D. Qiu, J. R. Dahn, *J. Electrochem. Soc.* **2015**, *162*, A1401.
- [49] M. M. Ma, N. A. Chernova, B. H. Toby, P. Y. Zavalij, M. S. Whittingham, *J. Power Sources* **2007**, *165*, 517.
- [50] M. Aykol, S. Kim, C. Wolverton, *J. Phys. Chem. C* **2015**, *119*, 19053.
- [51] X. S. Liu, W. L. Yang, Z. Liu, *Adv. Mater.* **2014**, *26*, 7710.
- [52] N. Schulz, R. Hausbrand, C. Wittich, L. Dimesso, W. Jaegermann, *J. Electrochem. Soc.* **2018**, *165*, A833.
- [53] R. Younesi, A. S. Christiansen, R. Scipioni, D. T. Ngo, S. B. Simonsen, K. Edstrom, J. Hjelm, P. Norby, *J. Electrochem. Soc.* **2015**, *162*, A1289.
- [54] I. Källquist, A. J. Naylor, C. Baur, J. Chable, J. Kullgren, M. Fichtner, K. Edström, D. Brandell, M. Hahlin, *Chem. Mater.* **2019**, *31*, 6084.
- [55] S. Malmgren, K. Ciosek, M. Hahlin, T. Gustafsson, M. Gorgoi, H. Rensmo, K. Edstrom, *Electrochim. Acta* **2013**, *97*, 23.
- [56] K. Edstrom, T. Gustafsson, J. O. Thomas, *Electrochim. Acta* **2004**, *50*, 397.
- [57] D. Pantea, H. Darmstadt, S. Kaliaguine, C. Roy, *Appl. Surf. Sci.* **2003**, *217*, 181.
- [58] L. Madec, R. Petibon, J. Xia, J. P. Sun, I. G. Hil, I. J. R. Dahn, *J. Electrochem. Soc.* **2015**, *162*, A2635.
- [59] L. Ma, J. Self, M. Y. Nie, S. Glazier, D. Y. Wang, Y. S. Lin, J. R. Dahn, *J. Power Sources* **2015**, *299*, 130.
- [60] R. Dedryvere, S. Leroy, H. Martinez, F. Blanchard, D. Lemordant, D. Gonbeau, *J. Phys. Chem. B* **2006**, *110*, 12986.
- [61] D. Aurbach, B. Markovsky, A. Shechter, Y. EinEli, H. Cohen, *J. Electrochem. Soc.* **1996**, *143*, 3809.
- [62] F. G. Zhao, G. Zhao, X. H. Liu, C. W. Ge, J. T. Wang, B. L. Li, Q. G. Wang, W. S. Li, Q. Y. Chen, *J. Mater. Chem. A* **2014**, *2*, 8782.
- [63] Y. G. Lei, K. M. Ng, L. T. Weng, C. M. Chan, L. Li, *Surf. Interface Anal.* **2003**, *35*, 852.
- [64] B. Philippe, R. Dedryvere, M. Gorgoi, H. Rensmo, D. Gonbeau, K. Edstrom, *J. Am. Chem. Soc.* **2013**, *135*, 9829.
- [65] A. Blidberg, T. Gustafsson, C. Tengstedt, F. Bjorefors, W. R. Brant, *Chem. Mater.* **2017**, *29*, 7159.
- [66] L. Painter, E. Arakawa, M. Williams, J. Ashley, *Radiat. Res.* **1980**, *83*, 1.
- [67] C. J. Powell, A. Jablonski, *NIST Electron Inelastic-Mean-Free-Path Database 71, Version 1.0*, NIST, Gaithersburg, MD **1999**.